

Cellular-resolution X-ray microtomography of an entire mouse brain

Mattia Humbel^{a,b}, Christine Tanner^{*a,b,c}, Marta Girona Alarcón^d, Georg Schulz^{a,b,c}, Timm Weitkamp^e, Mario Scheel^e, Vartan Kurtcuoglu^d, Bert Müller^{a,b}, Griffin Rodgers^{a,b}

^aBiomaterials Science Center, Department of Biomedical Engineering, University of Basel, Hegenheimermattweg 167B/C, 4123 Allschwil, Switzerland

^bBiomaterials Science Center, Department of Clinical Research, University Hospital Basel, Spitalstrasse 8/12, 4031 Basel, Switzerland

^cCore Facility Micro- and Nanotomography, Department of Biomedical Engineering, University of Basel, Hegenheimermattweg 167B/C, 4123 Allschwil, Switzerland

^dThe Interface Group, Institute of Physiology, University of Zurich, Winterthurerstrasse 190, 8057 Zurich, Switzerland

^eSynchrotron SOLEIL, L'Orme des Merisiers, 91190 Saint-Aubin, France

ABSTRACT.

Purpose: Histology is the gold standard for sub-cellular visualization of the mouse brain. It offers excellent in-plane resolution, but a comparably low out-of-plane resolution due to physical sectioning. X-ray microtomography does not require this trade-off. Tomographic imaging of the entire mouse brain with isotropic cellular resolution produces datasets of multiple terabytes in size. These data must be processed and made accessible to domain experts who may have only limited image processing knowledge.

Approach: Extended-field X-ray microtomography covering an entire mouse brain was performed. The 4,495 projections from 8×8 offset acquisitions were stitched to reconstruct a volume of $15,000^3$ voxels. The microtomography volume was non-rigidly registered to the Allen Mouse Brain Common Coordinate Framework v3 based on a combination of image intensity and landmark pairs.

Results: We present a 3.3 teravoxel dataset covering a full mouse brain with $0.65 \mu\text{m}$ voxel size. The data were block-wise transformed to a common coordinate system, then stored in a public repository with a hierarchical format for navigation and overlay with anatomical annotations in online viewers such as Neuroglancer or siibra-explorer.

Conclusions: This study demonstrates X-ray imaging and data processing for a full mouse brain, augmenting current atlases by improving resolution in the third dimension by an order of magnitude. The data are publicly available and easily accessible for domain experts via browser-based viewers.

Keywords: neuroimaging, X-ray histology, extended field-of-view, big data, registration, multi-resolution open data.

*Address all correspondence to Christine Tanner, christine.tanner@unibas.ch

1 Introduction

Neuroimaging is critical for decoding the brain's structure-function relationship.¹ However, even for smaller mammals such as mice, comprehensive brain mapping requires imaging on length scales spanning multiple orders of magnitude. For example, the width of the entire mouse brain is on the order of 1 cm, the size of cells is typically $1\text{--}10 \mu\text{m}$, synaptic connections can be thinner than 100 nm, and morphological changes on the order of a few nm can affect brain circuit function.¹ Therefore, a combination of imaging techniques are used to visualize the three-dimensional cytoarchitecture of the brain. Among these, virtual histology based on X-ray microtomography holds promise as a *post mortem* modality that can provide volumetric brain imaging with isotropic micron resolution.²⁻⁷ With techniques such as X-ray nanoholotomography, the resolution can be

pushed even below 100 nm.⁸ However, current results mostly explore regions of interest on the order of tens of cubic millimeters, while the entire mouse brain encompasses 500 mm³ of volume.⁹ Thus, the extension of microtomography to full-brain mapping has generated considerable interest in recent years.^{10–14}

While the penetration depth of hard X-rays through soft tissue is fully compatible with microtomography of centimeter-sized brains, the field-of-view (FOV) is typically limited by detector array size. Standard detector arrays consist of a few thousand pixels in each direction, e.g. the Hamamatsu Orca Flash 4.0 V2 currently employed at the ANATOMIX beamline of Synchrotron SOLEIL^{15,16} consists of a 2,048 × 2,048 array of 6.5 μm-wide pixels. Using 10× magnification and a single detector FOV, 0.65 μm pixel size and a maximum resolution of 1.5 μm can be achieved with a cylindrical FOV of 1.3 mm height and 1.3 mm diameter. Such local tomography scans already hold rich microanatomical information (see, e.g. Fig. 1 in Rodgers *et al.*¹⁷). The detector FOV can effectively be doubled by laterally positioning the rotation axis close to the edge of the detector, acquiring projections over 360°, and stitching projections 180° apart (see Fig. 1a). Such an off-axis acquisition with this instrument configuration can extend the reconstructed volume to 1.3 mm height, 2.5 mm diameter. However, the volume of the mouse brain is still about 70× larger. Therefore, the FOV must be still substantially extended for brain mapping.

Translation of the sample along the axis of rotation allows for extension of FOV *via* helical scans or, more commonly, stitching reconstructions from several height steps. Extending the FOV orthogonal to the rotation axis can be accomplished by either stitching reconstructions of local tomography scans,^{12,18} or building stitched projections with a common center-of-rotation (COR) prior to reconstruction (sometimes called a *mosaic* scheme).^{10,19} The former allows for standard reconstruction provided by most microtomography beamlines, though corrections are needed for common local tomography artefacts from truncated sinograms,^{20–22} and dedicated software for non-rigid stitching is required if the sample is deformed during acquisition.¹² The second approach is considered to be more dose- and time-efficient,¹¹ though it requires a dedicated pipeline for stitching of projections and reconstruction of large datasets.^{10,13,19}

The reconstruction of an entire mouse brain with 0.65 μm-wide voxels at 16-bit intensity resolution will result in a dataset of at least 3 TB in size. Sharing such a large image with the neuroscience community brings challenges in terms of data access, navigation, registration, and segmentation. To leverage existing brain atlas annotations and thus allow the community to better navigate the large dataset, the microtomography volume must be registered to an atlas. Yet registration of such large images often leads to problems, as the images and their spatial transformation exceed memory limits and/or cause excessive runtimes. To address these issues, we developed a distributed multi-resolution approach, where the large images are divided hierarchically into regions to circumvent memory limitations. This approach was used to register a multi-terabyte sized microtomography volume to the Allen Mouse Brain Common Coordinate Framework v3 (CCFv3).²³

The effective sharing of research data within multidisciplinary communities requires easy access and interpretability. For imaging data, this ideally means online tools for visualizing, sharing, and annotating images instead of large repositories with only data download options. Recently, interactive visualization platforms have been developed for displaying volumes of mega- to petavoxel size, including the `siibra-explorer`²⁴ and `Neuroglancer`.²⁵ The `siibra-explorer` is a browser-based viewer for brain atlases, which allows seamless querying of semantically and spatially anchored datasets thanks to tight integration with the Human Brain Project Knowledge Graph. `Neuroglancer` is a multi-resolution viewer capable of displaying tera- to petavoxel large

datasets and their segmentations fast enough to be practical. It enables easy collaboration, as any view can be shared by copying the uniform resource locator (URL) from the web browser, and as open-source software it is highly extensible. Its usefulness for collaborative brain studies has been demonstrated for example for segmenting the [full adult fly brain](#) dataset at $4 \times 4 \times 40$ nm resolution, resulting in 115 TB of image data.²⁶ Given these promising properties, we converted the registered microtomography volume of an entire mouse brain to the efficient pre-computed `Neuroglancer` format, which can also be read by the `siibra-explorer`, and then uploaded it to EBRAINS²⁷ for dissemination.

This work builds on the reconstruction pipeline for extended field-of-view tomographic reconstruction of entire organs with cellular resolution initially presented by Rodgers and co-workers.¹⁷ Here we report on (i) the acquisition of a large microtomography volume of an entire mouse brain with pixel size of $0.65 \mu\text{m}$ and its (ii) reconstruction, (iii) registration to the Allen Mouse Brain CCFv3 atlas, (iv) conversion to hierarchical `Neuroglancer` format for fast interactive visualization and access, and (v) dissemination via the EBRAINS Data and Knowledge services. The combination of all these aspects enables efficient sharing of the microtomography volume of the entire mouse brain with micrometer resolution in all three spatial dimensions.

2 Materials and Methods

2.1 Animals and tissue preparation

One wild-type twelve-week-old female C57BL/6JRj mouse (Janvier Labs, Le Genest-Saint-Isle, France) was transcardially perfused with 4% paraformaldehyde (PFA; Merck, Darmstadt, Germany) / phosphate buffered saline (PBS) pH 7.4 under Ketamine/Xylazine anesthesia, the brain dissected and then immersed in 4% PFA / PBS over night. Tissue collection was approved by the veterinary office of the Canton of Bern (license BE98/2020). For tissue dehydration, the brain was immersed for two hours in 20 mL each of 50%, 70%, 80%, 90% and 100% ethanol (Carl Roth GmbH, Karlsruhe, Germany). The brain was measured in 100% ethanol to take advantage of enhanced contrast from ethanol dehydration.^{28–31}

2.2 Extended-field microtomography acquisition

Imaging was performed at the ANATOMIX beamline at Synchrotron SOLEIL (Saint-Aubin, France).^{15,16} A filtered white beam with effective mean photon energy of around 38 keV was attained by setting the undulator gap to 5.5 mm and inserting $26 \mu\text{m}$ Au on $600 \mu\text{m}$ diamond and $100 \mu\text{m}$ Cu filters into the beam path. The detector consisted of a $20 \mu\text{m}$ -thick LuAG scintillator coupled to a scientific CMOS camera (Hamamatsu Orca Flash 4.0 V2, $2,048 \times 2,048$ pixels, $6.5 \mu\text{m}$ physical pixel size) *via* a Mitutoyo microscope objective ($10\times$, NA 0.28) resulting in an effective pixel size of $0.65 \mu\text{m}$.³² The detector was placed 50 mm downstream of the sample to exploit propagation-based phase contrast. This distance is of the same order as the critical near-field distance $z_c = (2\Delta)^2/\lambda$, where Δ is pixel size and λ is wavelength, which ensures that blurring from propagation-based phase contrast does not exceed two pixels.³³ The exposure time was set to 100 ms to fill half of the detector’s dynamic range, which avoids saturating the detector to reduce the severity of ring artefacts.

To cover the full width of the mouse brain, the detector’s FOV had to be linearly extended by a factor of eight, which corresponds to a $64\times$ larger reconstructed area compared to a standard

acquisition. This was achieved with the acquisition of four rings, each consisting of a 360° scan with offset COR, see Fig. 1. The COR was offset by 0.6, 1.8, 3.0 and 4.2 mm for rings 1, 2, 3 and 4, respectively. Note that in this convention, zero (0 mm) corresponds to the COR at the center of the detector FOV. Each ring scan consisted of 9,000 projections over 360° (4,495 over 180°). The acquisition of each ring took around 900 seconds using fly scan mode. Note that precision tilt alignment of the rotation stage must be better than 0.004° , as a reconstructed slice is only $0.65\ \mu\text{m}$ thick but 10 mm wide.

A total of eight height steps were needed to cover the mouse brain from cerebellum to olfactory bulbs. Height steps were acquired with offset of 1.2 mm, corresponding to an overlap of about 200 pixels. The total scan time was slightly over eight hours. Exemplary stitched projections are shown in Fig. 1c and d.

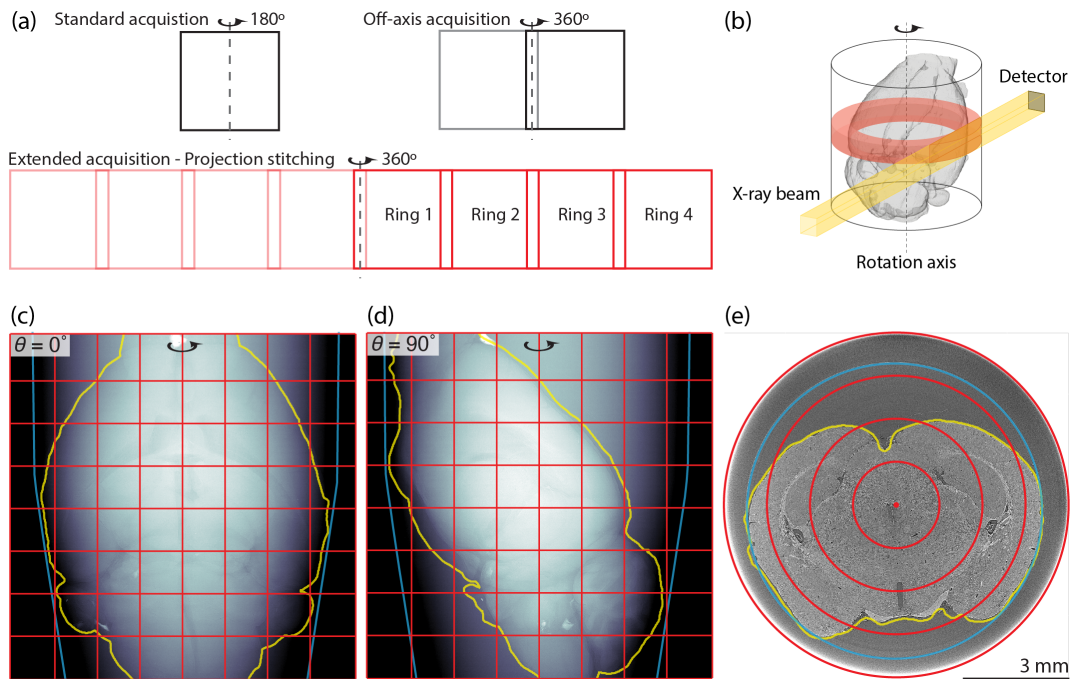


Fig. 1 Acquisition for large field-of-view (FOV) X-ray microtomography. Conventionally, microtomography scans rely on acquisition of one (a, top left) or two detector FOVs (a, top right). FOV can be extended perpendicular to the rotation axis by acquiring projections in concentric rings (a, bottom). The rotation axis is displaced relative to the detector and the X-ray beam to successively illuminate the entire cross-sectional area (b). An exemplary stitched projection is shown at 0° and 90° rotation angles for the acquisition of the mouse brain with 8×8 -times extended FOVs (c and d). Red lines delineate single $2,048 \times 2,048$ -pixel detector FOVs that were combined with an overlap of 200 pixels to form a single $14,982 \times 14,982$ -pixel projection. A reconstructed slice is shown with corresponding stitching positions in red (e). Yellow lines indicate the outline of the mouse brain and blue lines indicate the inner wall of the Eppendorf container used as a sample holder (c-e).

2.3 Reconstruction of extended field-of-view tomography data

Tomographic reconstruction was performed using an in-house developed pipeline with three main steps: (i) determination of the COR and ring overlap positions; (ii) projection blending, ring arte-

fact correction, and filtering for phase retrieval and/or noise reduction; and (iii) tomographic reconstruction. The pipeline was designed to run as batch jobs on either standard workstations or scientific computing infrastructure, e.g. with sciCORE³⁴ at the University of Basel, Switzerland. Note that this reconstruction pipeline is not the one available at the ANATOMIX beamline, which provides options for standard and off-axis reconstructions, but not for extended-field processing.

2.3.1 Center-of-rotation and overlap positions

The COR was found by maximizing cross-correlation in overlapping regions of projection pairs from the inner ring with rotation angles 180° apart. The mouse brain sample had relatively low contrast in projections, therefore ten flat-field corrected projection pairs were used to increase robustness. Peaks in the cross-correlation curves were automatically identified and their prominence determined with the `Matlab` function `findpeaks`. The COR was selected from the prominence-weighted average positions of these peaks. Overlap positions between rings and height steps were also found by maximizing cross-correlation in overlapping regions of projections from adjacent acquisitions. Again, prominence-weighted average peak positions from ten flat-field corrected projection pairs were used to increase robustness. The recorded motor positions of the translation stage were used as an initial estimate to limit the search range for both COR and overlap positions between rings.

2.3.2 Projection blending, ring artefact correction, and filtering of radiographic projections

Using the determined COR and overlap positions, single FOV projections were flat-field corrected and then combined with linear blending, i.e. $I_{\text{blend}} = \alpha I_i + (1 - \alpha) I_{i+1}$ with $\alpha \in [0, 1]$ linearly increasing through the overlap region, to create 8×8 extended projections around 180° of rotation. After blending, projections were filtered using Paganin's filter.³⁵

Ring artefacts were severe when no additional correction was applied. The correction was based on the mean of flat-field corrected projections over all rotation angles. This mean projection contained spot-like features that were the result of inhomogeneities that remained in fixed positions on the detector during acquisition. These inhomogeneities, which may have been caused by detector non-linearity, were the source of ring artefacts because they could not be fully removed by flat-field correction. The mean projection was high-pass filtered to isolate the ring artefact sources, which were then subtracted from all projections prior to reconstruction.

It is critical to select suitable parameters for both ring correction and filtering *before* reconstruction of teravoxel-sized datasets. Previews were generated by processing projections covering the full sample width but cropped in height to a stripe of, e.g., 32 pixels. This allowed for selection of the high-pass filter for ring correction and the δ/β ratio in Paganin's filter.³⁵ For this mouse brain, a ratio of $\delta/\beta = 140$ was chosen based on visual inspection of the reconstructions, considering the trade-off between contrast and spatial resolution.³⁶ Note that the filter was modified to remove multiplication by the factor $1/\mu$ (see Eq. 3 in Weitkamp *et al.*³³). This enables the interpretation of reconstructed values as linear attenuation coefficient.

The flat-field corrected, filtered, and blended projections were written to image files. The full mouse brain consisted of 4,495 projections of size $14,982 \times 14,982$, resulting in a data size of about $4,495 \times 900 \text{ MB} = 4 \text{ TB}$ at 32-bit floating-point precision prior to reconstruction. The projections were saved in Tagged Image File Format (TIFF) with tiling such that $14,982 \times 32$ strips could be quickly read for block-wise reconstruction.

2.3.3 Tomographic reconstruction

Reconstruction was performed on blocks of 32 sinograms to avoid excessive memory consumption and allow for parallelization. The open-source Python library `tomopy` (version 1.4.2)³⁷ was selected for its implementation of the *gridrec* reconstruction algorithm.^{38,39} The reconstruction section of the pipeline was thus written in Python (version 3.7.4). It reads a block of sinograms, takes the negative logarithm, performs tomographic reconstruction with `tomopy`'s *gridrec*, then crops, re-scales, and saves the reconstructed slices as a stack of TIFF images.

2.4 Registration to Allen Mouse Brain Common Coordinate Framework

Registration is an important tool for analysis of neuroimaging data and generation of brain atlases. Three-dimensional registration, particularly non-rigid registration, requires significant computational resources. For example, in a recent study, non-rigid registration of the full mouse brain required downsampling to 9.3 μm -wide voxels and limiting the number of transformation parameters to one displacement vector per 12^3 voxel volume.^{30,40}

We addressed these challenges by developing a distributed hierarchical approach with sub-volume registration for the full resolution steps, as illustrated in Fig. 2. First, volumes are downsampled to a size such that they and the required transformation files fit into memory during image registration. Image registration is then performed for these low-resolution volumes. The resulting transformation provides the corresponding coordinates in the moving space, which can be used to define corresponding local regions (Fig. 2, middle row). Regions of interest in the full-resolution volumes can then be transformed based on the low-resolution registration results (as in Fig. 2, bottom row) and/or independently registered if the degree of downsampling precludes accurate registration of fine anatomical structures.

This pipeline was employed for registering the microtomography volume to the template image of the Allen Mouse Brain CCFv3,²³ namely a hemisphere symmetric population average volume generated from two-photon microscopy images of 1,675 mice brains. For image registration, we used the open-source software `elastix`^{41,42} (version 5.0), as it provides standard registration functionalities as well as further useful features such as definition of image regions to be registered and the incorporation of landmark correspondences in the optimization function.

The tomography data was $32 \times 32 \times 32$ downsampled, i.e. 20.8 μm isotropic voxels, to approximate the resolution of the atlas, i.e. 25.0 μm isotropic voxels. Volumes were first manually aligned via a similarity transformation using `ITK-SNAP`⁴³ (version 3.8.0). To tune and guide registration, two observers each manually selected 35 corresponding landmark pairs \mathbf{L}_F and \mathbf{L}_M , where subscripts F and M denote fixed and moving image space, respectively. These landmarks from both observers were split into two equally sized sets to perform two-fold cross-validation to determine suitable registration meta-parameters. Besides the image volumes, i.e. the fixed atlas template \mathbf{V}_F and the moving microtomography \mathbf{V}_M , the usefulness of including image gradient magnitudes $|\nabla \mathbf{V}_F|$ and $|\nabla \mathbf{V}_M|$, as well as full brain segmentations \mathbf{S}_F and \mathbf{S}_M in a multi-image, multi-metric registration was tested. Thus, the spatial transformation T was determined by minimizing the cost function C :

$$C = f_{\text{-MI}}(\mathbf{I}_F, T(\mathbf{I}_M)) + w_G f_{\text{MSD}}(|\nabla \mathbf{V}_F|, T(|\nabla \mathbf{V}_M|)) + w_S f_{\text{-KS}}(\mathbf{S}_F, T(\mathbf{S}_M)) + w_L f_D(T(\mathbf{L}_F), \mathbf{L}_M) + w_T f_{\text{BE}}(T)$$

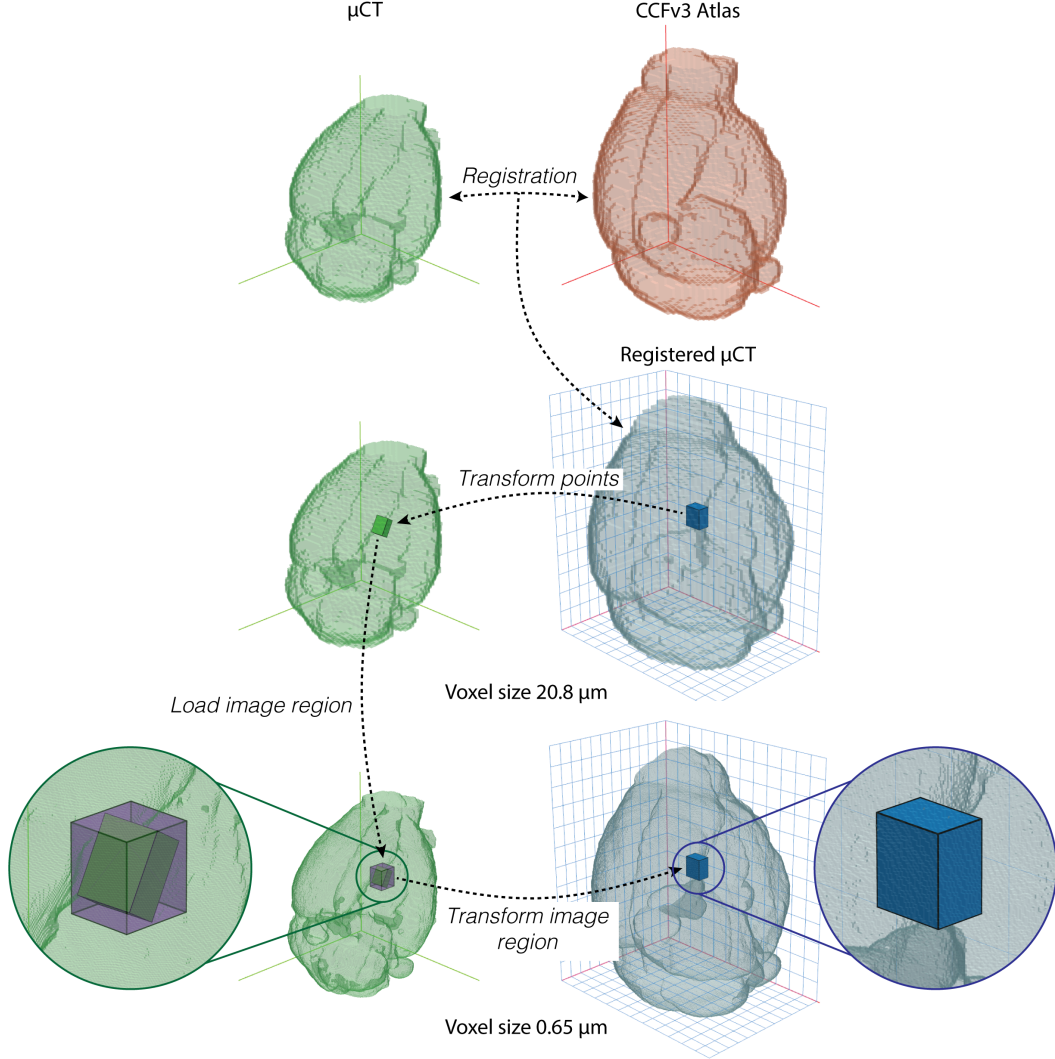


Fig. 2 Illustration of the distributed hierarchical 3D image registration and transformation framework. (top) Registration was performed with the $32\times$ downsampled microtomography (μ CT) images to fit in available memory and have a resolution similar to that of the atlas. (middle) Given an axes-aligned local image region in atlas space (blue box), the resulting spatial transformation provided the corresponding coordinates in the μ CT image space (green box). (bottom) Local transformation of the original μ CT image was then performed by loading only the axis-aligned image region (purple box), which encloses the potentially skewed green box. Repeating this procedure for all $12 \times 12 \times 12$ local regions in the reference space created the registered μ CT image.

The cost function C includes terms for negative mutual information f_{-MI} , mean squared difference f_{MSD} , negative Kappa statistics f_{-KS} , and mean Euclidean distance f_D , as well as a bending energy penalty f_{BE} for regularization. To include the brain boundaries, image dissimilarity measures f_{-MI} , f_{MSD} and f_{-KS} were determined for an extended brain region, i.e. within S_F and S_M dilated by a sphere of radius ten voxels. We tested the usefulness of incorporating $|\nabla V|$ and S in the registration, since the image gradient magnitudes will guide the local alignment of edges and the segmentations will support global alignment. The image dissimilarity measures were chosen to account for the nature of the image relationships. Firstly, negative mutual information f_{-MI} accounts for the nonlinear statistical relationship between X-ray microtomography and the CCFv3

atlas template’s two-photon microscopy intensity values. Secondly, mean squared difference f_{MSD} ensures edge alignment. Thirdly, negative Kappa statistics $f_{-\text{KS}}$ maximizes agreement between binary segmentations.

Registration was based on manual alignment with a similarity transform, followed by automatic affine and then deformable registration using a grid of control points with a spacing of s voxels interpolated with cubic B-Splines. Based on initial tests and the relative values of the cost functions, the registration meta-parameters were tested in the following ranges: $w_{|\nabla V|} \in \{0, 10^{-8}\}$, $w_S \in \{0, 1\}$, $w_L \in \{0, 0.1, 1\}$, $w_T \in \{1, 10, 100, 1,000, 10,000, 100,000\}$, and $s \in \{32, 16\}$. Finally, the images were registered using 70 landmarks and registration meta-parameters providing the lowest mean error for both cross-validation folds.

The full resolution tomography volume (moving volume) was warped to the atlas (fixed volume) by dividing the fixed space into $12 \times 12 \times 12$ target subregions, such that the axes-aligned extended moving image subregion (purple bounding box in bottom row of Fig. 2), the moving image transformed subregion (blue box in bottom row of Fig. 2), and the transformation parameters all fit in memory for an isotropic target voxel resolution of $0.65 \mu\text{m}$.

2.5 Visualization and sharing of TB-sized data

For dissemination and exploration of the registered data, `siibra-explorer` and `Neuroglancer` were used. `Neuroglancer` is an open-source browser-based interactive visualization platform that allows for datasets up to petabyte size.²⁵ The warped image regions were transformed to gzipped chunks of $64 \times 64 \times 64$ voxels in sharded pre-computed `Neuroglancer` format at six resolution levels, i.e. $0.65, 1.3, 2.6, 5.2, 10.4$ and $20.8 \mu\text{m}$ for efficient visualization. The `sharded format` combines all chunks into a fixed number of larger shard files to avoid the performance penalties incurred by many small files. The sharded chunks were produced using the open-source software `Igneous` (version 4.19.2).⁴⁴ The pre-computed data were uploaded to an EBRAINS repository, where it can be publicly accessed with the `siibra-explorer` or the `Neuroglancer` viewer using the corresponding URL. In `siibra-explorer`, users can navigate to more than 1,300 predefined Allen Mouse Brain CCFv3 regions by their anatomical names using the underlying hierarchical ontology.²³ The data can also be accessed and processed by suitable software including `CloudVolume`⁴⁵ in combination with `Igneous`.

3 Results and Discussion

3.1 The full mouse brain dataset

The full mouse brain, defined here to include the cerebellum, but not the olfactory bulbs, was scanned with eight height steps, see Fig. 1c and d (caudal part of olfactory bulbs at top, top of brain stem at the bottom). The resulting stitched dataset contained $14,982 \times 14,982 \times 14,784$ voxels, or 3.3 teravoxels. At 16-bit precision, this corresponds to a data size of 6.6 TB. It should be noted that this reflects the entire reconstructed FOV of 911 mm^3 . Re-orienting and cropping to more closely cover the approximately 500 mm^3 volume of the mouse brain would reduce data size.

Figure 3 shows an overview rendering of the entire mouse brain data with $8\times$ downsampling. Virtual horizontal sectioning as in Fig. 3 (right) reveals macroscopic regions such as the isocortex, olfactory areas, hippocampal formation, cerebral nuclei, fiber tracts, and cerebellum. The full-resolution data provide in-plane details similar to conventional histology, but with the benefit of

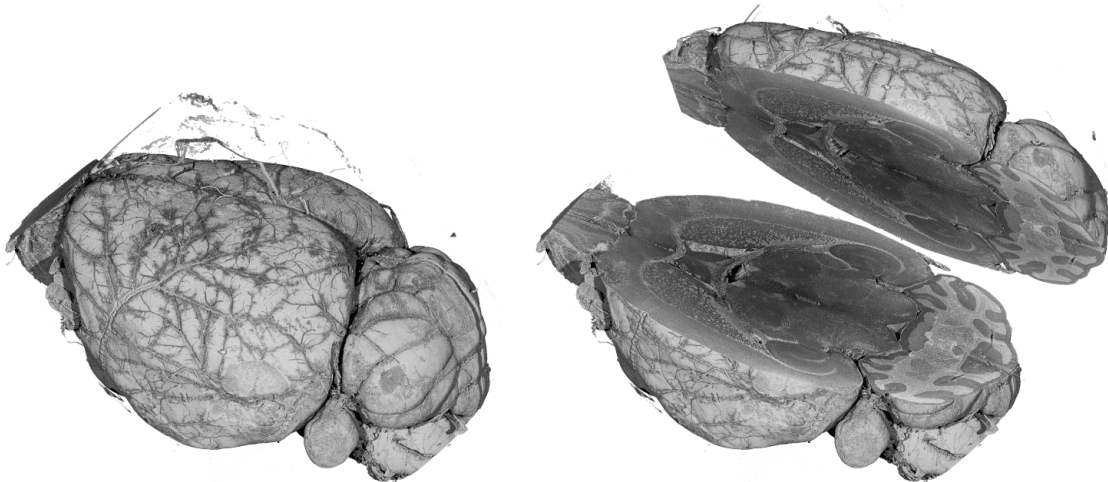


Fig. 3 Volume rendering of the reconstructed mouse brain dataset. Volumetric imaging with isotropic resolution allows for exploration of the brain along any virtual slicing direction, here a horizontal slice is shown. Note that the rendering represents $8\times$ binned data, which has a size around 10 GB and can be handled by a standard workstation. Multi-resolution approaches are necessary for these teravoxel datasets. Volume renderings were made with VGStudio MAX 2.1 (Volume Graphics, Heidelberg, Germany). From Rodgers *et al.*¹⁷ with permission.

three-dimensional isotropic resolution. This allows for exploration of the volumetric data in any virtual slicing plane. Fig. 4 is a rendering of a virtual coronal section of the full-resolution data revealing anatomical microstructures such as fiber tracts, vessels, and individual cells. Three-dimensional cellular structures can be explored in the isotropic resolution data, for example the complex surface of the choroid plexus is clearly visualized in Fig. 4 (right).

3.2 Registration to Allen Mouse Brain Common Coordinate Framework

Table 1 lists the mean registration errors from two-fold cross-validation based on 70 manually selected landmark pairs. Results are shown for the configuration achieving the lowest errors for affine and non-rigid registration as well as the best configuration when excluding image gradients ($w_{|\nabla V|} = 0$), segmentations ($w_S = 0$), and/or landmarks ($w_L = 0$). Lowest errors were achieved for affine and non-rigid registration when landmarks were incorporated into the cost function, i.e. $w_L > 0$. The weights providing the lowest mean error for the two-fold cross-validation, i.e. stated in last two columns in Table 1, were employed for the final registration. Note that the 70 selected landmarks were used without exception for the final registration.

The number of confidently identifiable landmark pairs was limited by anatomical variations as well as differences in structure appearances between the microtomography volume and the average two-photon microscopy CCFv3 template. Landmarks included ideal point landmarks as well as central positions of larger anatomical structures. Figure 5 shows image regions around a manually selected landmark from Observer 1 in the original images and after registration. After non-rigid registration, reasonable alignment of corresponding anatomical structures can be seen. The combination of intensity-based registration and landmark alignment with optimized weighting supported robustness against small errors in manual landmark positions. Further landmarks and their alignment after registration can be seen in Fig. 6.

Figure 7 shows virtual slices from the atlas template image and the non-rigidly registered microtomography volume. The resulting alignment enables the observation of similarities and dif-

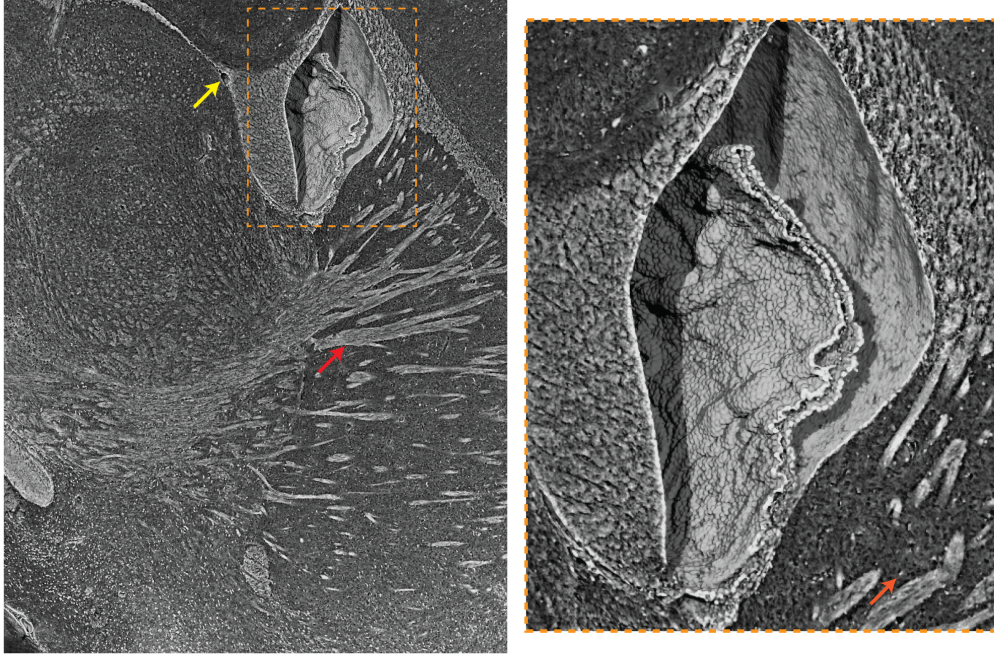


Fig. 4 Volume rendering of a virtual coronal section from the full resolution mouse brain data. Three-dimensional cellular structures can be explored in the isotropic resolution data including fiber tracts (red), vessels (yellow), and individual cells (orange, right). For example, magnified views of the lateral ventricle (right) show the complex surface of the choroid plexus. The orange dashed box is 1.1 mm high.

Table 1 Accuracy of image registration based on landmark error f_D from two-fold cross-validation are given for weight configurations of image gradient ($w_{|\nabla V|}$), segmentation (w_S), and landmarks (w_L). For non-rigid registration, meta-parameters include bending energy penalty weight (w_{BE}) and grid spacing (s) in voxels. The lowest mean landmark error of 0.08 mm was achieved for non-rigid registration with the configuration shown in the last column (grey). The other columns listed the best configurations when excluding image gradients ($w_{|\nabla V|} = 0$), segmentations ($w_S = 0$), and/or landmarks ($w_L = 0$). For comparison, the mean landmark error after manual pre-alignment was 2.49 mm.

	Affine registration						Non-rigid registration					
$w_{ \nabla V }$	0	10^{-8}	10^{-8}	0	10^{-8}	10^{-8}	0	10^{-8}	10^{-8}	0	10^{-8}	10^{-8}
w_S	0	0	1	0	0	1	0	0	1	0	0	1
w_L	0	0	0	1	1	1	0	0	0	0.1	0.1	0.1
w_{BE}	-	-	-	-	-	-	100	1000	100	1000	1000	1000
s	-	-	-	-	-	-	16	16	16	16	16	16
f_D [mm]	0.25	0.16	0.16	0.14	0.14	0.14	0.40	0.13	0.13	0.09	0.08	0.08

ferences in anatomy and appearance of structures. Due to the ill-posed problem of registering multi-modal data across mice, the alignment is in some places imperfect. Yet, the alignment is sufficient to provide an understanding of the shown anatomical structures when overlaid with the atlas segmentation. Thus, the present registration is useful for general alignment with the Allen

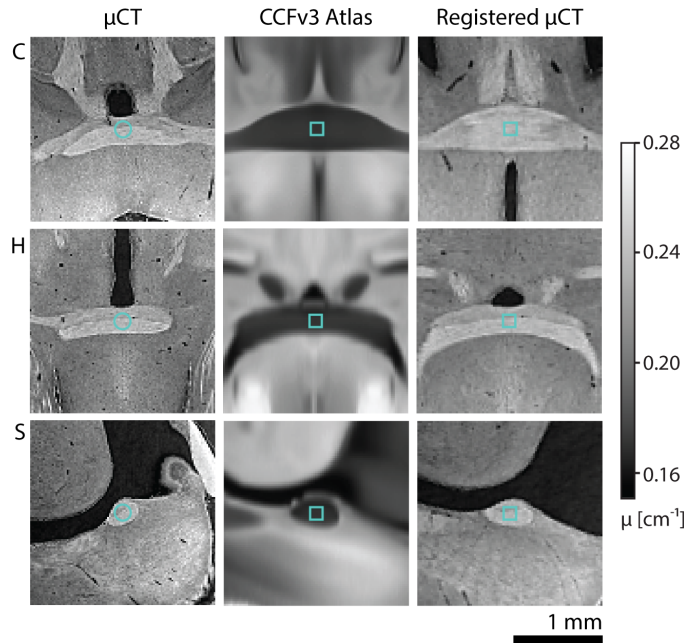


Fig. 5 Registration results at corresponding landmark positions in the original microtomography (μ CT), the atlas, and the non-rigidly registered μ CT datasets are displayed in virtual coronal (C), horizontal (H), and sagittal (S) planes. Representative landmark pairs selected by Observer 1 (turquoise). Image intensities for the μ CT and the two-photon microscopy-based template of the Allen Mouse Brain CCFv3 atlas were scaled to [1, 99] percentile of pixel intensities. The color bar indicating the linear attenuation coefficient μ applies to the μ CT images.

Mouse Brain CCFv3 atlas and navigation, but labels should not be transferred from the atlas without further refinement.

In the Allen Mouse Brain CCFv3 template, the whole brain volume is 506 mm^3 . This is because the underlying serial two-photon data of formalin-fixed agarose-immersed brains were scaled to match the unfixed fresh-frozen Nissl-based template of CCFv1.²³ This achieved backward compatibility and closeness in volume to *in vivo* mouse brains.⁴⁶ The mean brain volume in the original serial two-photon data used for the CCFv3 template was 435 mm^3 .²³ By comparison, transforming the CCFv3 template to the coordinate frame of our mouse brain dataset in 100 % ethanol produces a volume of 244 mm^3 . The local change in volume as a result of non-rigid registration is shown in the right column of Fig. 7. A smooth shrinkage pattern with a mean volumetric strain of -48% can be observed, with larger shrinkage on the outside of the brain. We previously observed a median volumetric strain of -39% from formalin to ethanol embedding,³⁰ which here would correspond to an estimated volume of 400 mm^3 in formalin and thereby falls within the range of volumes reported for the 1,675 mouse brains used for the CCFv3 template.

3.3 Visualization and sharing of TB-sized data

Details of microanatomical structures of the registered microtomography volume are shown in Fig. 8 for the hippocampal and striatum dorsal region. At the highest resolution, cells, fibers, and other microscopic structures are clearly visible. The displayed virtual slices were downloaded from the publicly available dataset via CloudVolume, demonstrating that this dataset can not only be viewed, but also downloaded for processing.

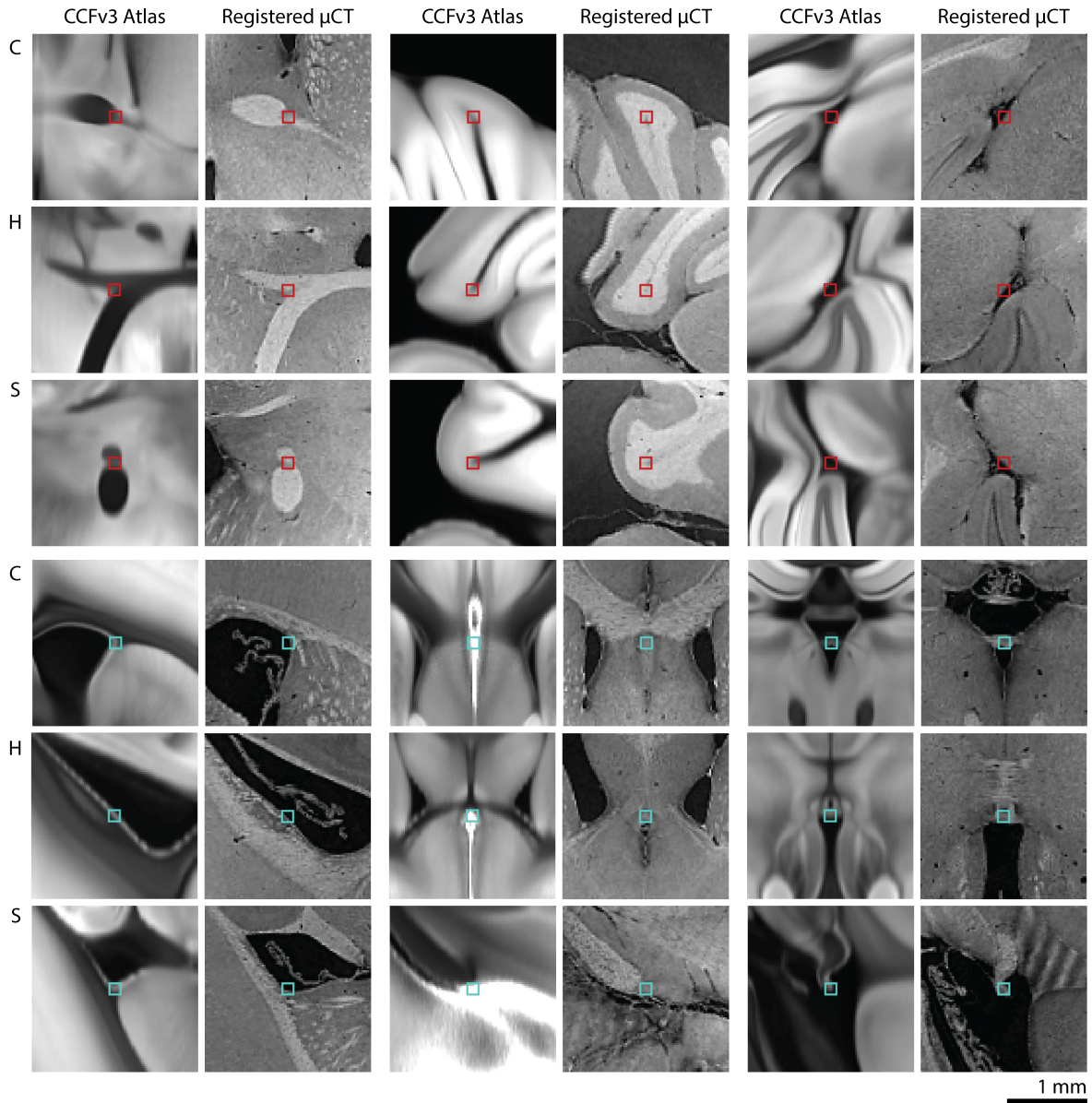


Fig. 6 Registration results at corresponding landmark positions in the Allen Mouse Brain CCFv3 atlas and the non-rigidly registered microtomography (μ CT) datasets are displayed in virtual coronal (C), horizontal (H), and sagittal (S) planes. Representative landmark pairs selected by Observer 1 (bottom, turquoise) and Observer 2 (top, red) are shown. Image intensities for the μ CT and the two-photon microscopy-based template of the Allen Mouse Brain CCFv3 atlas were scaled to [1, 99] percentile of pixel intensities.

The conversion to sharded chunks instead of raw chunks, both of chunk size $64 \times 64 \times 64$ voxels, reduced the number of required files for six resolutions (0.65 to 20.8 μ m) substantially from 20,312,064 to 4,959. Intensity values were stored as 16-bit integers. These can be converted to linear attenuation coefficients by mapping the grayscale intensity range $[0, 65,535]$ to $[-0.01 \text{ mm}^{-1}, 0.10 \text{ mm}^{-1}]$. Note that negative attenuation values are the result of edge enhancement that was not completely removed. The gzipped pre-computed data in Neuroglancer format required a total of 5.4 TB disk storage space. The complete multi-resolution data has been

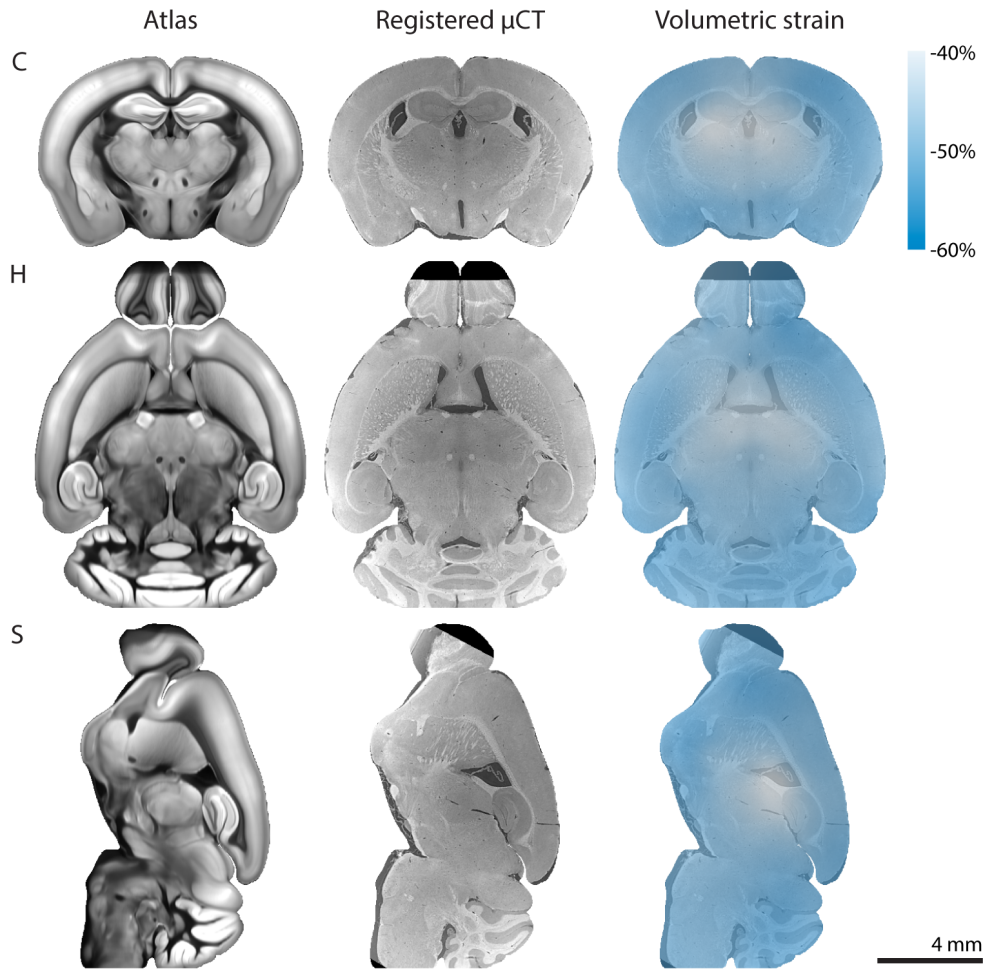


Fig. 7 Non-rigid registration results. Virtual coronal (C), horizontal (H), and sagittal (S) slices are shown from the two-photon microscopy-based template of the Allen Mouse Brain CCFv3 atlas,²³ the non-rigidly registered microtomography (μ CT) volume, and the volumetric strain as a result of registration.

uploaded to a publicly accessible EBRAINS repository⁴⁷ and can be viewed via the `siibra-explorer` using [this URL](#) and in Neuroglancer using [this URL](#).^{*} Note that both viewers allow encoding the position when sharing a URL, in this case located in the caudoputamen. Six resolution levels, in conjunction with the precomputed Neuroglancer format with data chunks of $64 \times 64 \times 64$ voxels, allow fast interactive viewing via `siibra-explorer` or Neuroglancer by loading only the required chunks at the appropriate image resolution. This eases navigation to microanatomical details and keeping the macroscopic overview. Figure 9 illustrates the visualization of the warped microtomography image in `siibra-explorer`. The correspondence between the microtomography volume and the two-photon template image of the Allen Mouse Brain CCFv3 can be observed. The microtomography image structures can be explored by navigating to predefined brain regions of the Allen Mouse Brain CCFv3 such as the parabrachial nucleus.

^{*}Note, the EBRAINS repository is under embargo until acceptance of this manuscript. Currently the URL links to view the data in `siibra-explorer` and Neuroglancer, stated in the text and in the caption of Fig. 9, point to open data including only the two lowest resolutions at 10.4 and $20.8 \mu\text{m}$ voxel size. These URL links will be updated to the high resolution data in the final version of the manuscript.

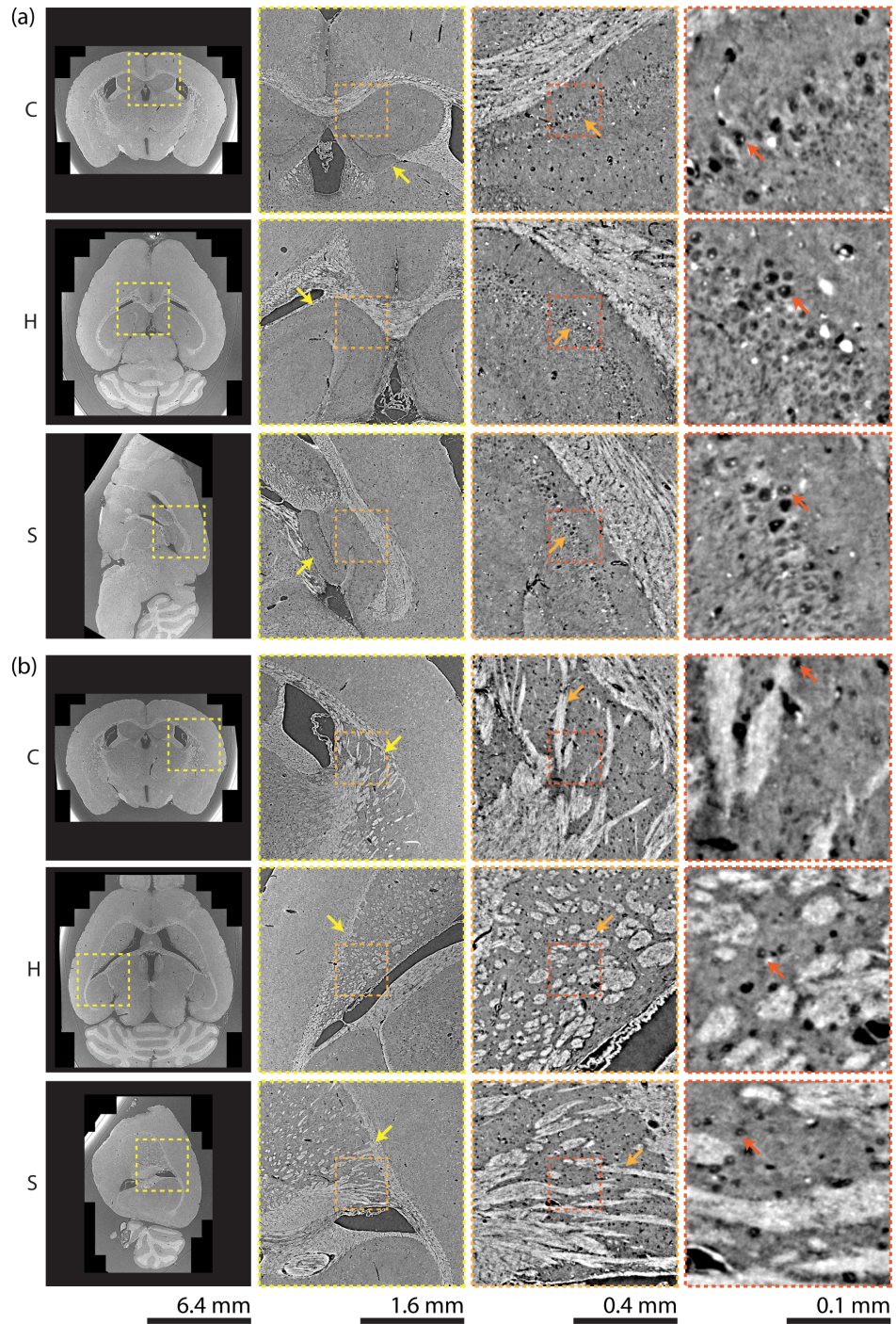


Fig. 8 Microanatomical details from the (a) hippocampal and (b) striatum dorsal regions are shown in orthogonal virtual coronal (C), horizontal (H), and sagittal (S) slices of the microtomography volume registered to the Allen Mouse Brain CCFv3 atlas. (a) Magnified views reveal structures of increasing detail, with arrows indicating (yellow) the hippocampus (including dentate gyrus and Ammon's horn), (orange) the CA1 field of the Ammon's horn, and (red) the nucleus of an individual pyramidal neuron. (b) Details from the striatum dorsal region are shown with arrows indicating (yellow) caudoputamen, (orange) fiber tracts, and (red) the nucleus of a single neuron. Multi-resolution datasets are publicly shared in zipped pre-computed Neuroglancer format.

Illustration of browser-based Siibra-explorer:
Sub-micron μ CT with atlas label overlay

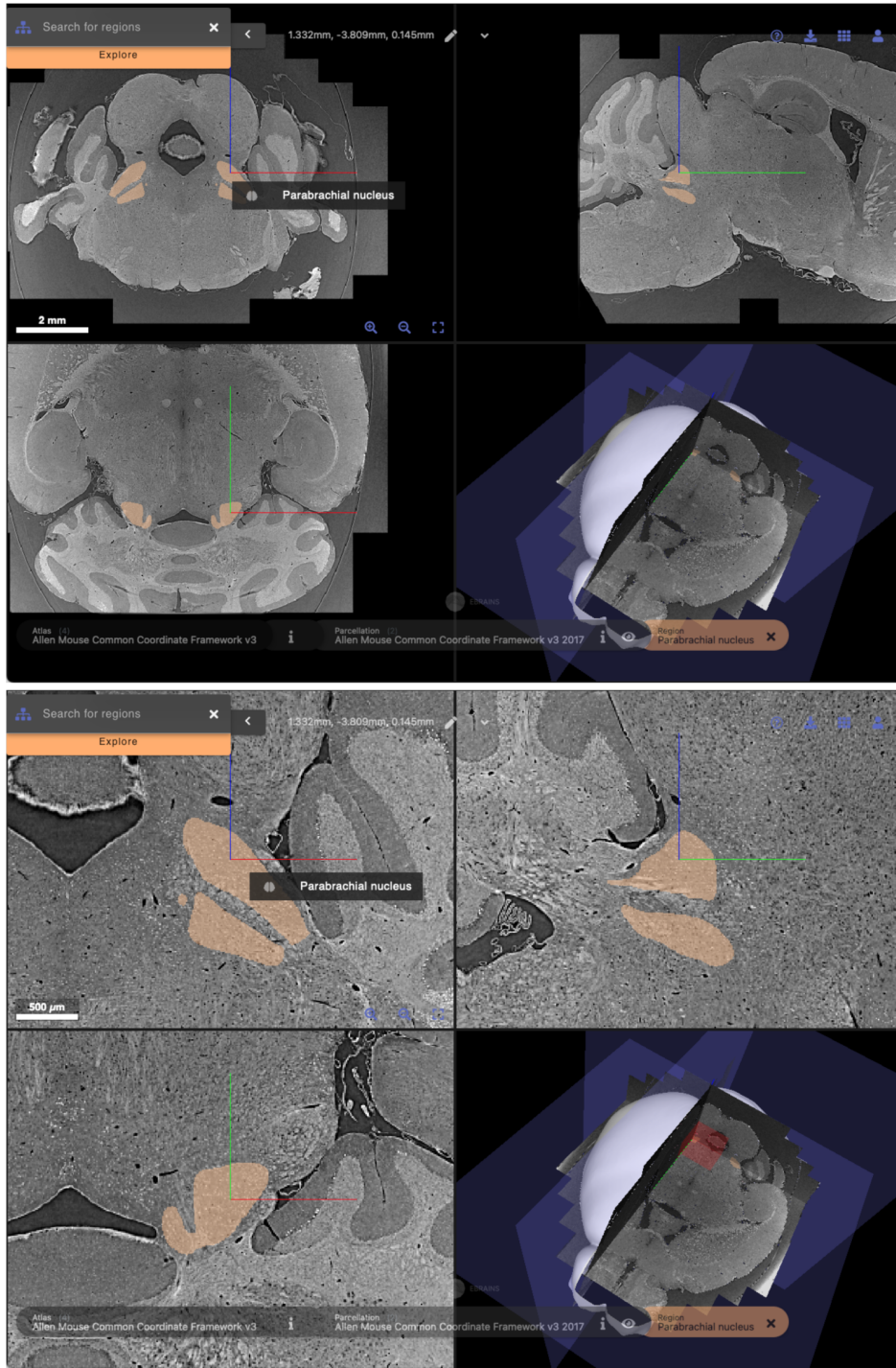


Fig. 9 Browser-based navigation of the publicly available mouse brain dataset. Visualization of microtomography image in the *siibra-explorer* is demonstrated with an overlaid segmentation of the parabrachial nucleus region from the Allen Mouse Brain CCFv3. The multi-resolution viewer allows for exploring the full dataset at lower resolutions (top), while still loading the full-resolution data at higher magnifications (bottom). Data are available at [this URL](#).

4 Conclusion

Virtual histology based on extended-field X-ray microtomography provides isotropic micrometer resolution with fields-of-view capable of encompassing more than an entire mouse brain. The dataset presented here provides rich microanatomical detail and form a basis for novel analyses. Overcoming barriers in sharing, viewing, navigating, and combining these data with existing resources will unlock collaborations with domain experts who may have limited experience in handling teravoxel-sized imaging data. In this study, we introduced a dedicated data processing pipeline to manage terabyte-sized virtual histology datasets and integrate them with open-source interactive viewers. The reconstructed tomography data were registered and transformed into a common coordinate system, then made accessible through an online repository in a hierarchical format for exploration via web browser-based viewers. Crucially, the data's compatibility with tools like `siibra-explorer` and `Neuroglancer` allows users to use existing labels from other datasets to rapidly identify areas of interest, overlay the microtomography volumes with images from other modalities, and share specific location coordinates via URL, facilitating collaboration with peers.

Disclosures

The authors declare no conflicts of interest.

Code, Data, and Materials Availability

The data presented in this article are publicly available via the EBRAINS repository with DOI [10.25493/759K-JVU](https://doi.org/10.25493/759K-JVU).

The source code for software used for tomographic reconstruction is available at the Github repository [mosaicreconstruction](#). Raw data for the tomographic acquisition are available from Synchrotron SOLEIL via the user portal [SUN set](#), project number 20201710, as described in the parameters accompanying the tomographic reconstruction software. The source code for software used for large volume transformations is available at the Github repository [LargeVolumeTransformix](#). The downsampled microtomography dataset, masks, landmarks, registration parameters, transformation files as well as the scripts used for formatting the transformed volume for the browser-based viewers are available at the Zenodo repository DOI [10.5281/zenodo.10992465](https://doi.org/10.5281/zenodo.10992465).

Acknowledgments

The authors thank Dr. G. Enzmann and Prof. Dr. B. Engelhardt of the Theodor Kocher Institute, University of Bern, Switzerland, for providing the animals, performing the perfusion, and dissecting the brains. The authors thank the curation team of EBRAINS and X. Gui from the Forschungszentrum Jülich GmbH, Germany, for their prompt and efficient support in curating and integrating the data to the `siibra-explorer`.

Beamtime at the ANATOMIX beamline was granted by Synchrotron SOLEIL under proposal 20190424. ANATOMIX is an Equipment of Excellence (EQUIPEX) funded by the Investments for the Future program of the French National Research Agency (ANR), project NanoimagesX, grant no. ANR-11-EQPX-0031. Calculations were performed at [sciCORE](#) scientific computing center at University of Basel, Switzerland. V.K. acknowledges support from the Swiss National Science Foundation *via* NCCR Kidney.CH and project no. 182683. V.K. and M.G. acknowledge

financial support from the Swiss National Science Foundation project no. 213535. M.H., C.T., B.M. and G.R. acknowledge financial support from the Swiss National Science Foundation project no. 185058.

References

- 1 J. W. Lichtman and W. Denk, “The big and the small: Challenges of imaging the brain’s circuits,” *Science* **334**, 618–623 (2011).
- 2 A. Khimchenko, H. Deyhle, G. Schulz, *et al.*, “Extending two-dimensional histology into the third dimension through conventional micro computed tomography,” *NeuroImage* **139**, 26–36 (2016).
- 3 S. E. Hieber, C. Bikis, A. Khimchenko, *et al.*, “Tomographic brain imaging with nucleolar detail and automatic cell counting,” *Scientific Reports* **6**, 32156 (2016).
- 4 E. L. Dyer, W. G. Roncal, J. A. Prasad, *et al.*, “Quantifying mesoscale neuroanatomy using X-ray microtomography,” *eNeuro* **4**, e0195–17.2017 (2017).
- 5 M. Töpperwien, F. van der Meer, C. Stadelmann, *et al.*, “Three-dimensional virtual histology of human cerebellum by X-ray phase-contrast tomography,” *Proceedings of the National Academy of Sciences* **115**, 6940–6945 (2018).
- 6 M. Töpperwien, F. van der Meer, C. Stadelmann, *et al.*, “Correlative x-ray phase-contrast tomography and histology of human brain tissue affected by Alzheimer’s disease,” *NeuroImage* **210**, 116523 (2020).
- 7 M. Chourrout, C. Sandt, T. Weitkamp, *et al.*, “Virtual histology of Alzheimer’s disease: Biometal entrapment within amyloid- β plaques allows for detection via X-ray phase-contrast imaging,” *Acta Biomaterialia* **170**, 260–272 (2023).
- 8 A. Khimchenko, C. Bikis, A. Pacureanu, *et al.*, “Hard X-Ray Nanoholotomography: Large-Scale, Label-Free, 3D Neuroimaging beyond Optical Limit,” *Advanced Science* **5**(6), 1700694 (2018).
- 9 Y. Ma, P. R. Hof, S. C. Grant, *et al.*, “A three-dimensional digital atlas database of the adult C57BL/6J mouse brain by magnetic resonance microscopy,” *Neuroscience* **135**, 1203–1215 (2005).
- 10 R. Vescovi, M. Du, V. de Andrade, *et al.*, “Tomosaic: Efficient acquisition and reconstruction of teravoxel tomography data using limited-size synchrotron X-ray beams,” *Journal of Synchrotron Radiation* **25**, 1478–1489 (2018).
- 11 M. Du, R. Vescovi, K. Fezzaa, *et al.*, “X-ray tomography of extended objects: A comparison of data acquisition approaches,” *Journal of the Optical Society of America A* **35**, 1871–1879 (2018).
- 12 A. Miettinen, I. V. Oikonomidis, A. Bonnin, *et al.*, “NRStitcher: Non-rigid stitching of terapixel-scale volumetric images,” *Bioinformatics* **35**, 5290–5297 (2019).
- 13 N. T. Vo, R. C. Atwood, M. Drakopoulos, *et al.*, “Data processing methods and data acquisition for samples larger than the field of view in parallel-beam tomography,” *Optics Express* **29**, 17849–17874 (2021).
- 14 S. Foxley, V. Sampathkumar, V. De Andrade, *et al.*, “Multi-modal imaging of a single mouse brain over five orders of magnitude of resolution,” *NeuroImage* **238**, 118250 (2021).
- 15 T. Weitkamp, M. Scheel, J. L. Giorgetta, *et al.*, “The tomography beamline ANATOMIX at Synchrotron SOLEIL,” *Journal of Physics: Conference Series* **849**, 012037 (2017).

- 16 T. Weitkamp, M. Scheel, J. Perrin, *et al.*, “Microtomography on the ANATOMIX beamline at Synchrotron SOLEIL,” in *Journal of Physics: Conference Series*, **2380**, 012122 (2022).
- 17 G. Rodgers, C. Tanner, G. Schulz, *et al.*, “Mosaic microtomography of a full mouse brain with sub-micron pixel size,” in *Developments in X-Ray Tomography XIV, Proceedings of SPIE* **12242**, 323–335 (2022).
- 18 A. Kyrieleis, M. Ibison, V. Titarenko, *et al.*, “Image stitching strategies for tomographic imaging of large objects at high resolution at synchrotron sources,” *Nuclear Instruments and Methods in Physics Research Section A: Accelerators, Spectrometers, Detectors and Associated Equipment* **607**, 677–684 (2009).
- 19 R. F. C. Vescovi, M. B. Cardoso, and E. X. Miqueles, “Radiography registration for mosaic tomography,” *Journal of Synchrotron Radiation* **24**, 686–694 (2017).
- 20 A. Kyrieleis, V. Titarenko, M. Ibison, *et al.*, “Region-of-interest tomography using filtered backprojection: Assessing the practical limits,” *Journal of Microscopy* **241**(1), 69–82 (2011).
- 21 J. C. da Silva, M. Guizar-Sicairos, M. Holler, *et al.*, “Quantitative region-of-interest tomography using variable field of view,” *Optics Express* **26**, 16752–16768 (2018).
- 22 A.-L. Robisch, J. Frohn, and T. Salditt, “Iterative micro-tomography of biopsy samples from truncated projections with quantitative gray values,” *Physics in Medicine & Biology* **65**, 235034 (2020).
- 23 Q. Wang, S.-L. Ding, Y. Li, *et al.*, “The Allen mouse brain common coordinate framework: A 3D reference atlas,” *Cell* **181**, 936–953.e20 (2020).
- 24 X. Gui, fsdavid, C. Schiffer, *et al.*, “FZJ-INM1-BDA/siibra-explorer,” (2023). v2.14.4, <https://doi.org/10.5281/zenodo.10390355>.
- 25 J. Maitin-Shepard, A. Baden, W. Silversmith, *et al.*, “google/neuroglancer,” (2021). v2.23, <https://doi.org/10.5281/zenodo.5573294>.
- 26 Z. Zheng, J. S. Lauritzen, E. Perlman, *et al.*, “A complete electron microscopy volume of the brain of adult *Drosophila melanogaster*,” *Cell* **174**(3), 730–743 (2018).
- 27 “EBRAINS.” <https://www.ebrains.eu/>. Accessed: 2024-04-17.
- 28 M. Töpperwien, A. Markus, F. Alves, *et al.*, “Contrast enhancement for visualizing neuronal cytoarchitecture by propagation-based x-ray phase-contrast tomography,” *NeuroImage* **199**, 70–80 (2019).
- 29 G. Rodgers, W. Kuo, G. Schulz, *et al.*, “Virtual histology of an entire mouse brain from formalin fixation to paraffin embedding. Part 1: Data acquisition, anatomical feature segmentation, tracking global volume and density changes,” *Journal of Neuroscience Methods* **364**, 109354 (2021).
- 30 G. Rodgers, C. Tanner, G. Schulz, *et al.*, “Virtual histology of an entire mouse brain from formalin fixation to paraffin embedding. Part 2: Volumetric strain fields and local contrast changes,” *Journal of Neuroscience Methods* **365**, 109385 (2022).
- 31 J. Brunet, C. L. Walsh, W. L. Wagner, *et al.*, “Preparation of large biological samples for high-resolution, hierarchical, synchrotron phase-contrast tomography with multimodal imaging compatibility,” *Nature Protocols* **18**, 1441–1461 (2023).
- 32 K. Desjardins, A. Carcy, J.-L. Giorgetta, *et al.*, “Design of indirect X-ray detectors for tomography on the Anatomix beamline,” in *Mechanical Eng. Design of Synchrotron Radiation Equipment and Instrumentation (MEDSI’18), Paris, France, 25-29 June 2018*, 355–357, JACOW Publishing, Geneva, Switzerland (2018).

- 33 T. Weitkamp, D. Haas, D. Wegrzynek, *et al.*, “ANKAphase: Software for single-distance phase retrieval from inline X-ray phase-contrast radiographs,” *Journal of Synchrotron Radiation* **18**, 617–629 (2011).
- 34 “sciCORE.” <https://scicore.unibas.ch/>. Accessed: 2024-04-17.
- 35 D. Paganin, S. C. Mayo, T. E. Gureyev, *et al.*, “Simultaneous phase and amplitude extraction from a single defocused image of a homogeneous object,” *Journal of Microscopy* **206**(1), 33–40 (2002).
- 36 G. Rodgers, G. Schulz, H. Deyhle, *et al.*, “Optimizing contrast and spatial resolution in hard x-ray tomography of medically relevant tissues,” *Applied Physics Letters* **116**, 023702 (2020).
- 37 D. Gürsoy, F. De Carlo, X. Xiao, *et al.*, “TomoPy: A framework for the analysis of synchrotron tomographic data,” *Journal of Synchrotron Radiation* **21**, 1188–1193 (2014).
- 38 B. A. Dowd, G. H. Campbell, R. B. Marr, *et al.*, “Developments in synchrotron x-ray computed microtomography at the National Synchrotron Light Source,” in *Developments in X-Ray Tomography II, Proceedings of SPIE* **3772**, 224–236 (1999).
- 39 M. L. Rivers, “tomoRecon: High-speed tomography reconstruction on workstations using multi-threading,” in *Developments in X-Ray Tomography VIII, Proceedings of SPIE* **8506**, 169–181 (2012).
- 40 G. Rodgers, G. Schulz, W. Kuo, *et al.*, “Non-rigid registration to determine strain fields during mouse brain fixation and embedding,” in *Bioinspiration, Biomimetics, and Bioreplication XI, Proceedings of SPIE* **11586**, 115860I (2021).
- 41 S. Klein, M. Staring, K. Murphy, *et al.*, “Elastix: A toolbox for intensity-based medical image registration,” *IEEE Transactions on Medical Imaging* **29**, 196–205 (2010).
- 42 D. Shamonin, E. Bron, B. Lelieveldt, *et al.*, “Fast parallel image registration on CPU and GPU for diagnostic classification of Alzheimer’s disease,” *Frontiers in Neuroinformatics* **7**, 50 (2014).
- 43 P. A. Yushkevich, Y. Gao, and G. Gerig, “ITK-SNAP: An interactive tool for semi-automatic segmentation of multi-modality biomedical images,” in *Int. Conf. of the IEEE Engineering in Medicine and Biology Society*, 3342–3345 (2016).
- 44 W. Silversmith, A. Zlateski, J. A. Bae, *et al.*, “Igneous: Distributed dense 3D segmentation meshing, neuron skeletonization, and hierarchical downsampling,” *Frontiers in Neural Circuits* **16**, 977700 (2022).
- 45 W. Silversmith, F. Collman, N. Kemnitz, *et al.*, “seung-lab/cloud-volume,” (2021). v5.3.2, <https://doi.org/10.5281/zenodo.5671443>.
- 46 Y. Ma, D. Smith, P. R. Hof, *et al.*, “In vivo 3D digital atlas database of the adult C57BL/6J mouse brain by magnetic resonance microscopy,” *Frontiers in Neuroanatomy* **2**, 175 (2008).
- 47 M. Humbel, C. Tanner, G. Schulz, *et al.*, “Mosaic microtomography of an entire mouse brain with sub-micron pixel size.” EBRAINS (2023). v1.0, <https://doi.org/10.25493/759K-JVU>.

Mattia Humbel has been a PhD student at the Biomaterials Science Center since June 2022. His research focuses on the three-dimensional imaging of brain tissue both in and ex vivo, with a special focus on extended field of view acquisition techniques and data processing. Previous work includes a study of nanostructures in dental composites using X-ray nanotomography and multiple scattering simulation. He received an MSc degree in physics from ETH Zürich in 2022.

Christine Tanner is senior scientist in medical image processing and data analysis. She worked for Siemens AG in Munich, Germany, as a software engineer for 12 years. In 1998, she graduated from the University of Edinburgh, United Kingdom, with a degree in artificial intelligence and mathematics. After a research MSc, she completed her part-time PhD at King's College London, United Kingdom, in 2005 on registration and lesion classification of magnetic resonance breast images. She then was a research fellow and lecturer at ETH Zürich, Switzerland, in the field of medical image analysis. In 2020, she joined the Biomaterials Science Center at the University of Basel, Switzerland, to support it in all aspects of quantitative information extraction from images.

Marta Girona Alarcón completed her BSc degree in Nanoscience and Nanotechnology at the Autonomous University of Barcelona, Spain, in 2017. She then obtained an MSc degree in Molecular Technologies from the University of Applied Sciences and Arts Northwestern Switzerland. Since 2019, she has been pursuing her PhD at the University of Zurich. Her research primarily focuses on employing synchrotron radiation-based computed tomography for in vivo and post-mortem imaging of the central nervous system.

Georg Schulz graduated in theoretical physics at the University of Freiburg, Germany, in 2008. Subsequently, he started his PhD project on the multimodal visualization of human brain at the University of Basel, Switzerland. He earned his doctoral degree in physics in 2012. Since 2012, he has been a research associate in the field of high-resolution hard X-ray imaging and has become responsible for the core facility micro- and nanotomography at the medical faculty of the University of Basel, Switzerland.

Timm Weitkamp received a PhD in physics from the University of Hamburg, Germany, in 2002. He has more than 25 years of experience in synchrotron radiation-based X-ray phase-contrast imaging. He is the head of the ANATOMIX micro- and nanotomography beamline at Synchrotron SOLEIL, the French national synchrotron light source. His research interests are X-ray optics, imaging and X-ray microscopy, and their applications in various fields of research from advanced materials and systems to biological and medical studies.

Mario Scheel holds a PhD in physics obtained in 2009 from the University of Göttingen. In more than 15 years of work in synchrotron X-ray imaging, he has acquired expertise over a wide range of techniques such as high-energy microtomography, inline phase-contrast imaging, and hard X-ray full-field transmission microscopy (TXM). As a scientist at the ANATOMIX tomography beamline at Synchrotron SOLEIL, he is in charge of the TXM nanotomography endstation, which he designed and built. He is also heavily involved in the application of his developments to areas such as materials science and biomedical research.

Vartan Kurtcuoglu received his PhD in biomedical engineering from ETH Zurich, Switzerland, in 2006. He holds the position of Associate Professor of Computational and Experimental Physiology at the University of Zurich, Institute of Physiology, where he heads The Interface Group. His primary research interests are the mechanisms of fluid flow and solute transport in biological systems, with a focus on the mammalian central nervous system its cerebrospinal fluid spaces.

Bert Müller holds the Thomas Straumann Chair for Materials Science in Medicine at the University of Basel, Switzerland, and is founding director of the Biomaterials Science Center. He received his MSc degree in physics from the Dresden University of Technology, Germany; his PhD in experimental physics from the University of Hannover, Germany; and his habilitation in

experimental physics from ETH Zurich, Switzerland. His current research interests include high-resolution hard X-ray imaging and physics-based approaches in medicine and dentistry. He is a Fellow of SPIE and the 2022 recipient of the SPIE Biophotonics Technology Innovator Award.

Griffin Rodgers received his BA in physics from the University of California, Berkeley in 2015, his MSc in physics from ETH Zürich in 2018, then completed a PhD in physics at the University of Basel in 2021 with doctoral thesis “Hard X-ray microtomography for virtual histology of the brain with cellular resolution”. After working as a postdoctoral researcher at the University of Basel, he joined Bottneuro AG in 2023 as a computational scientist.